The induction of angiogenesis by cerium oxide nanoparticles through the modulation of oxygen in intracellular environments

Soumen Das[1,#], Sanjay Singh[2,#], Janet M. Dowding[2], Saji Oommen[3], Amit Kumar[1], Thi X. T. Sayle[4], Shashank Saraf[1], Chitta Ranjan Patra[5], Nicholas E. Vlahakis[3], Dean C. Sayle[4], William T. Self[2], and Sudipta Seal[1,*]

[1]Department of Mechanical, Materials and Aerospace Engineering, Advanced Materials Processing Analysis Center, University of Central Florida, Orlando, Florida

[2]Burnett School of Biomedical Science, University of Central Florida, Orlando, Florida

[3]Div. Pulmonary & Critical Care, Mayo Clinic, Rochester, Minnesota, USA

[4]Department of Engineering and Applied Science, Cranfield University, Defence Academy of the United Kingdom, Shrivenham SN6 8LA, United Kingdom

[5]Department of Biochemistry and Molecular Biology Mayo Clinic College of Medicine, Rochester, Minnesota, USA

Abstract

Angiogenesis is the formation of new blood vessels from existing blood vessels and is critical for many physiological and pathophysiological processes. In this study we have shown the unique property of cerium oxide nanoparticle (CNPs) to induce angiogenesis, observed using both *in vitro* and *in vivo* model systems. In particular, CNPs trigger angiogenesis by modulating the intracellular oxygen environment and stabilizing hypoxia inducing factor 1α endogenously. Furthermore, correlations between angiogenesis induction and CNPs physicochemical properties including: surface Ce^{3+}/Ce^{4+} ratio, surface charge, size, and shape were also explored. High surface area and increased Ce^{3+}/Ce^{4+} ratio make CNPs more catalytically active towards regulating intracellular oxygen, which in turn led to more robust induction of angiogenesis. Atomistic simulation was also used, in partnership with in vitro and in vivo experimentation, to reveal that the surface reactivity of CNPs and facile oxygen transport promotes pro-angiogenesis.

Keywords

Cerium oxide nanoparticle; angiogenesis; hypoxia inducing factor 1α; intracellular oxygen concentration; molecular dynamics; surface reactivity

*Corresponding Author: Sudipta seal; Department of Mechanical, Materials and Aerospace Engineering, Advanced Materials Processing Analysis Center, 4000 Central Florida Blvd, Engineering I, Room Number 381, Orlando, FL 32816, USA, Sudipta.Seal@ucf.edu phone: (407) 823-5277, Fax: (407) 882-1156.
#Authors contribute equally

1. INTRODUCTION

Angiogenesis is a critical process, which leads to the formation of new blood vessels necessary for development and other physiological processes [1]. However, abnormal angiogenesis can trigger pathological conditions such as cancer, chronic inflammation, diabetic retinopathy and arthritis [2, 3]. In patients presenting chronic wounds or ischemic heart diseases, insufficient angiogenesis is a major pathological component. In these patients pro-angiogenic cytokines such as VEGF and bFGF have been proposed to increase the blood flow to the damaged area [3–5]. However, clinical trials with VEGF-A and other growth factors were not satisfactory and associated with pathological angiogenesis, thrombosis and fibrosis [3, 6]. Clearly, new methods and biomaterials to trigger angiogenesis are needed. Recently Eu(III) hydroxide nanorods have been reported to have pro-angiogenic properties [3, 7]. Similarly, cerium oxide nanoparticles (CNPs), another redox-active rare earth nanoparticle, have gained considerable interest because of their potential therapeutic applications [8]. Oxygen modulation and transport is pivotal to almost all biological processes and therefore an understanding of how nanomaterials might influence this important balance is fundamental.

To this end it is very interesting to explore how the solubility, size, shape (i.e. nanorods, particles, stars) and composition influences the surface reactivity, oxygen storage and ease of oxygen extraction and transport from the surface of the nanomaterial/biological interface. In particular, the oxygen buffering capacity of CNPs is well established [9, 10] and is attributed to the valence state of cerium combined with inherent defects in the crystal lattice structure, which are magnified at the nano-scale. The stability of HIF-1α, a transcription factor which regulates gene expression involved in angiogenesis, depends upon intracellular oxygen concentrations [11]. New strategies could therefore be developed to alter HIF-1α stabilization and promote angiogenesis by exploiting the oxygen buffering capacity of CNPs. Here, we have explored the pro-angiogenic properties of CNPs using both *in vitro* and *in vivo* assays.

2. MATERIALS AND METHODS

2.1 Preparation and characterization of Cerium oxide nanoparticle

Two different methods were adapted to prepared cerium oxide nanoparticles. Cerium nitrate hexahydrate (99.999% pure from Sigma Aldrich) were used as a precursor in both the preparation. Cerium oxide nanoparticles I (CNP I) have been prepared using wet chemical method as described previously [12]. Cerium oxide nanoparticle II (CNP II) was synthesized using NH_4OH precipitation method. Briefly, cerium nitrate hexahydrate were dissolved in deionized sterile water and stoichiometric amount NH_4OH was added and stirred for 4hr at room temperature. Cerium oxide nanoparticles were separated by centrifugation at 8000 g for 10 minutes. Size and morphology of the nanoparticle were analyzed using High resolution transmission electron microscopy (HRTEM), with FEI Tecnai F30 having an energy dispersive X-ray (EDX) analyzer. The oxidation states of the cerium on the surface of the nanoparticle were calculated using 5400 PHI ESCA (XPS) spectrometer and Mg-Kα X-radiation (1253.6 eV) at a power of 350watts was used during the data collection.

Different sized nanoparticles were procured from different sources; 10–15 nm from Alfa Aesar Inc; 15–20 nm from Nanostructure and amorphous Inc; <25nm from Sigma Aldrich Inc and 50–60 nm from Johnson Matthey Plc

2.2. Cell culture

HUVEC cells were obtained from Lonza Walkersville, Inc (Walkersville, MD, USA). HUVEC cells were grown in Endothelial Basal Media-2 (Lonza Walkersville) containing 2% FBS. Cultures were maintained at 37°C and 5% CO_2 in humidified incubator and only passages 3–6 were used for experiments.

2.3. Cell viability assay

The proliferation of HUVECs were assayed by colorimetric assay using MTT (3-(4,5 dimethylthiazol-2-yl)-2,5-diphenyl tetrazolium bromide) dye. Cells were cultured in 96-well plate at a density of 3×10^3 cells/well. Then cells were treated with different concentration of CNPs incubated for 24hr and 48hr. MTT was added to the cells at a final concentration of 1.2 mM and further incubated for 4hr. Cells were lysed and the insoluble formazan product was dissolved using buffer (10%SDS, 0.1M HCl) and the absorbance was measured at 570 nm using SpectraMax 190 spectrophometer (Molecular Devices, Sunnyvale, CA, USA). Cell proliferation was calculated by absorbing the CNPs treated samples/untreated control in percentage.

2.4. Endothelial tube formation assay

Growth factor reduced BD matrigel (BD Bioscience) was coated on a 96 well plate. 8.0– 10.0×10^3 endothelial (HUVEC) cells (passage 4–5) were plated per well. Cells were then treated with different concentrations of CNPs (10 nm to 10 μM). A positive control containing 30 ng/ml of rVEGF was used and a negative control was included the inhibitor 2-Methoxyestradiol. The numbers of tubes formed were calculated after 8hours using brightfield microscopy and experiments were included triplicate cultures and carried out three times to determine reproducibility.

2.5. CAM Assay

The CAM assay was performed as described previously [13, 14]. Chicken eggs were purchased from Charles River Laboratories, Franklin, CT and maintained in a humidified 39°C incubator (Lyon Electric, Chula Vista, CA). Pellets containing 0.5% methylcellulose plus recombinant human VEGF-A (50ng), CNP1 (1 μg) or CNP2 (1 μg) were placed onto the CAM of 10-day-old chick embryo. Eggs were subsequently incubated at 39°C and on Day 13 the CAM's were fixed and excised and then imaged using a digital camera (Canon PowerShot 6) attached to a stereomicroscope (Zeiss, Germany). Angiogenesis was quantified by counting the branch points arising from tertiary vessels from a minimum of 8 specimens from the three separate experiments.

2.6. DCFDHA staining

2500 cells/cover slip were seeded on a glass cover slip in a 6-well cell culture plate and allowed cells to adhere for 24 hrs. Fresh medium was then added with and without CNPs, as

well as positive and negative controls. Cells were then treated with 20 μM DCFDA and incubated for 30 min and washed with PBS. After washing cells were fixed under chilled methanol (−20 °C) for 8 min. Cells were again washed twice with PBS followed by incubation with DAPI for 8 min. Finally cells were washed and mounted in anti-fade mounting media (Calbiochem) and slides were prepared. These slides were stored at 4°C until imaging under Leica TCS SP5 laser scanning confocal microscope with 40 X oil objective lens.

2.7. Pimonidazole immunostaing

Pimonidazole staining was carried out as describe elsewhere [15]. HUVEC cells were grown on cover slips for overnight and then treated with 1 μM CNPI for 0 min (control), 30 min, 1 h, and 2 h. Then pimonidazole (final concentration 200 μM) was added to the cells and incubated for 45 min and cells were permeabilized/fixed with ice cold methanol for 10 min at room temperature and washed thoroughly with saline. Fixed cells were then blocked using 3 % BSA in saline. Then cells were stained with FITC-conjugated monoclonal Hypoxyprobe-1 monoclonal antibody 1 (mAb1) (1:100 in 3% BSA) for one hr at room temperature and DAPI were used to stained the nucleus. Finally, cells were washed and mounted in anti-fade mounting media (Calbiochem) and examined under Fluorescence microscope. Using Image J 1.44p software (Wayne Rasband, National Institute of Health, USA) fluorescence intensity of 20 individual cells/field and 10 different fields were estimated for each group and plotted as mean and standard deviation.

2.8. Western blots

HUVEC cells were seeded on 60 mm petri plates coated with growth factor reduced BD matrigel (BD biosciences). Following CNPs treatment at 0.5h, 2h and 4h or $CoCl_2$ (positive control) cells were recovered by BD cell recovery kit. NE_PER Nuclear and Cytoplasmic Extraction Kit (Thermo) were used to isolate nuclear and cytoplasmic extract. Proteins were measured using Bradford assay. Equal amount of protein (25 μg) were fractionated by 4–20 % SDS-PAGE gradient gels and transferred to PVDF membrane. 1:2000 diluted monoclonal anti-human VEGF and HIF1α antibody were used as primary antibody, incubated for overnight at 4°C. Anti-mouse IgG conjugated with HRP (1:15,000) used as 2ndary antibody, incubated for 1hr at room temperature. Chemiluminescence method was adopted for developing the blot. Equal loading were ensured re-probing of the blot using anti-β-actin antibody (1:1000). Densitometry analysis (ImageJ Software) was also carried out from the image to have semi quantitative data of HIF-1α nuclear translocation.

2.9. ELISA assay for VEGF

Growth factor reduced BD matrigel (BD Bioscience) was coated on a 96 well plate. 8.0–10.0 × 10^3 endothelial (HUVEC) cells (passage 4–5) were plated per well as describe in endothelial tube formation assay. Then cells were treated with different concentration of CNPs and culture media were collected after 8 h of incubation with nanoparticles. Amount of VEGF in culture media were assayed using ELISA kit (Bio Scientific Corporation) following manufacturer's instructions.

2.10. RT PCR

Changes in gene expression following CNP treatment, if any, were analyzed using real-time reverse transcriptase polymerase chain reaction (RT-PCR) as a function of time with or without exposure to CNP. Briefly, the total RNA was extracted, and an equal quantity of mRNA (0.5 μg) was used for cDNA synthesis using Iscript cDNA synthesis kit (Bio-Rad). Oligonucleotides were designed using Primer3 Software (simgene.com). RT-PCR was carried out using Bio-Rad ICycler (Biomolecular Science Center) using SYBR green dye. Up-regulation or down-regulation of each mRNA was calculated from C_T values using GAPDH as an internal standard. The oligonucleotides used are shown in Table 1.

2.11. Simulation

In this section we describe the potential model used to represent the interactions between the Ce and O atoms together with the strategy used to generate the atomistic model of the nanoparticle.

2.11.1. Simulation code and potential models—The DL_POLY code was used to perform all the molecular dynamics (MD) simulations [16]; the user manual provides comprehensive analytical descriptions and discussion of the molecular dynamics simulations, force fields, boundary conditions, algorithms and parallelisation methods used in these simulations; three-dimensional periodic boundary conditions were imposed throughout.

All calculations were based upon the Born model of the ionic solid, where the energy, E, of the system is given by:

$$E(r_{ij}) = \sum_{ij} \frac{Q_i Q_j}{4\pi\varepsilon_o r_{ij}} + \sum_{ij} A\exp\left(\frac{-r_{ij}}{\rho}\right) - C r_{ij}^{-6},$$

the first term represents the Coulombic interaction between ion *i* of charge Q_i and ion *j* of charge Q_j, which are a distance r_{ij} apart. This functional form is very slowly convergent and therefore the Ewald summation, with an accuracy of 10^{-6}, was used to increase the speed of convergence and reduce computational cost. The second term is of the Buckingham form, which is particularly effective in representing ionic solids. Model parameters,[17] used to describe CeO_2, are presented in Table 2. Interionic potential parameters, of the form:

$$E(r_{ij}) = \sum_{ij} \frac{Q_i Q_j}{4\pi\varepsilon_o r_{ij}} + \sum_{ij} A\exp\left(\frac{-r_{ij}}{\rho}\right) - C r_{ij}^{-6}$$, used to describe the ceria.

2.11.2. Generating the atomistic model—To generate the atomistic model of the ceria nanoparticle, a cube of ceria, comprising 24696 atoms, was cleaved from the parent material. The cube was positioned in a simulation cell with lattice parameters sufficiently large to prevent any interaction between neighbouring (image) nanoparticles. The nanoparticle was first amorphised, by performing constant volume MD simulation at 8000 K for 50 ps, and then crystallised by performing constant volume MD simulation at 3750 K, for 2500 ps. Finally, the nanoparticle was cooled by performing MD simulation at 1K for

sufficient a duration to converge the energy. The final model thus represents a low energy configuration for a ceria nanoparticle. Such procedures have been documented previously [18].

To generate the reduced nanoparticle, two Ce(IV) ions at the surface were reduced to Ce(III) and an oxygen atom removed to ensure charge neutrality. Constant volume MD simulation was performed at 1 K for sufficient a duration to converge the energy and resulted in a model for the low-temperature structure of a reduced ceria nanoparticle. $CeO_2\{100\}$ surfaces have been shown to be chemically more reactive compared to {111} [19] and therefore the oxygen vacancy was created on one of the {100} surfaces with two neighbouring Ce(IV) reduced to Ce(III). Our calculations revealed that it is easier (energetically) to reduce Ce(IV) on a {100} surface compared to a {111} surface. The electrostatic potential of all the oxygen species was then calculated to determine labile surface oxygen.

An additional calculation was performed whereby a high concentration of Ce^{3+}, together with charge compensating oxygen vacancies, were introduced at the surface of the ceria nanoparticle and the ease of oxygen extraction, to participate in the catalytic cycle, calculated. In particular, 1000 Ce^{4+} at the surface of an amorphous CeO_2 nanoparticle comprising 24696 ions were reduced to Ce^{3+} and 500 oxygen vacancies created by removing 500 oxygen ions from the surface. The nanoparticle was then crystallised at 2400 K for 7500 ps and cooled to OK. The electrostatic potential was then calculated for the low-temperature structure.

2.11.3. Statistical analysis—Results are expressed as the mean±SD. Data were analyzed by one way ANOVA using GraphPad Prism version 5.00 for Windows (GraphPad Software, San Diego California USA).

3. RESULT AND DISCUSSION

3.1. Characterization of CNPs

Herein, we have engineered CNPs with varying Ce^{3+}/Ce^{4+} ratio's, termed CNP I and CNP II, respectively. Figure 1A shows the particle sizes of both types of nanoparticles averaging 3–5 nm in size. Figure 1B–D show the Ce (3d) XPS spectrum of CNPI and CNPII. CNPI has a high Ce^{3+} concentration (57 %) as compared to CNPII (27 %), calculated as described elsewhere [20]. Measured Zeta potentials of CNPI and CNPII are (+) 17.78±0.5 and (−) 14.05±0.83 mV, respectively (Figure 1E). For comparison we **obtained** different sized CNPs (10–15, 15–20, <25 and 50–60 nm) from various sources. CNPs with different shapes including stars[21], polygonals[22], and nanorods[23] have also been synthesized and confirmed by HRTEM (Figure 1S; supplementary document).

3.2. Physiochemical properties of CNPs and endothelial tube formation

Proliferation of endothelial cells is the critical first step involved in angiogenesis [24]. Therefore, proliferation of the human umbilical vein endothelial cells (HUVECs) was estimated using the tetrazolium dye reduction (MTT) assay. No cytotoxicity was observed in cells exposed to either of the CNPs (Figure S2 A & B; Supplementary document). Cell

proliferation was also analyzed in the presence of different size and shaped CNPs at a concentration of 1 μM (Figure S2 C & D; Supplementary document). With the exception of ceria nanorods, other size and shaped nanoparticles did not reveal any overt toxicity towards HUVEC cells; exposure to ceria nanorods led to a slight reduction in cell proliferation ($P > 0.05$).

The endothelial tube formation assay is an *in vitro* model system where anti and pro-angiogenic molecules can be tested [25]. Figure 2(A) shows the representative tube formation of the control, positive control (30 ng VEGF), negative control (10 μM 2-methoxyestradiol) and different concentrations of CNPI exposure. Interestingly, we observed that the addition of CNPI to cells resulted in a significant, concentration dependent, induction of tube formation up to 1 μM (P 0.0001; ~ 40% increase). Further, concentration increases of CNPI up to 10 μM do not increase tube formation significantly (data not shown). A weaker induction of tube formation was seen (P 0.05; ~11% increase) with the addition of CNPII (Figure 2B). To confirm that tube formation induction is a unique property of CNPs, a similar sized SiO_2 nanoparticle (5–10 nm; Figure S1; supplementary document) was tested and no tubes were observed (Figure 3A). We also determined Lipopolysaccharide (LPS) contamination, because low levels of LPS may influence the tube formation assay. LPS was not detected using either of the CNPs (<0.005 EU/ml), **indicating** that induction of tube formation is an intrinsic property of CNPs.

As engineered, the main difference between CNPI and CNPII is the surface Ce^{3+}/Ce^{4+} ratio. However, they also vary in surface charge: CNPI is positively charged, and CNPII is negatively charged (Figure 1E). To confirm whether tube formation induction is a function of surface charge, we tested the effect of tube formation using CNPI and CNPII with inverted surface charge by treating the nanoparticles with acid (1 mM HCL) or alkali (1 mM NaOH) and solutions were kept stirring for 4–6hr. After thorough washing with dH_2O, the inverted zeta potential of CNPI* and CNPII* was altered to -20 ± 1.4 mV and $+44.08 \pm 1.1$ mV, respectively. No difference in tube formation induction was noticed when cells were treated with the original CNPs or surface charged altered CNPs (Figure 3B).

Since during tube formation CNPs have been incubated in ECM (endothelial cell culture media) we explored whether ECM influences the CNPs surface charge. Both preparations were analyzed after 1hr incubation in ECM in the absence of cells and both types of nanoparticles showed a net negative surface charge of about $(-)$ 9.23±0.56 mV, which revealed that nanoparticles interact with components of ECM which shifts the surface charge to negative. Our combined results indicate that surface charge does not influence tube induction.

It is well known that size and shape can influence the catalytic activity of CNPs [9]. To determine possible size and shape effect, CNPs spanning: 3–5, 10–15, 15–20, >25 and 50–60 nm were exposed to HUVECS at a concentration of 1 μM. Only 3–5 nm and 10–15 nm sized CNPs showed induced tube formation. Exposing HUVECs to CeO_2 particles >15 nm in size did not result in tube formation (Figure 3C). Moreover, micron size particles inhibited tube formation, though inhibition was not statistically significant. It is well known that the catalytically active surface area of nanoparticles decreases with increase in particle

size and therefore perhaps unsurprising those nanoparticles >15 nm did not influence tube formation. However, it is disingenuous to ignore size effects completely, because size modulation may also be linked to a mechanistic change by which the cells interact with nanoparticles. To eliminate this possibility, HUVECs were exposed to different shaped CNPs (all >15 nm); no discernible difference in tube formation was observed as a function of shape (Figure 3D).

3.3. CNPs and vascular sprouting in CAM assay

To support our observations using tube assays, we performed chick CAM sprouting assays. Figures 4A–D represents the CAM after treatment with vehicle (A), VEGF (positive control) (B), 1 μM CNPI (C) or 1 μM CNPII (D). No vascular sprouting was observed when CAMs were treated with water only (control). Vascular sprouting was observed with CAMs, treated with VEGF (50 ng), as expected. Similarly, the CAMs treated with CNPI remarkably also show significant, robust vascular sprouting. Specifically, CNPI promotes angiogenesis (P 0.001) with matured vascular sprouting; CNPII (P 0.001) also presents similar angiogenesis but is less robust compared to CNPI. Quantitative data from the CAM assay is shown in Figure 4E and reveals that CNPI induces a 400 % increase in angiogenesis compared to the unstimulated control. Our results clearly demonstrate that CNPs induce endothelial cell proliferation as well as vascular sprouting.

3.4. Regulation of VEGF, HIF1α and intracellular oxygen environment

Next, we analyzed VEGF expression in culture media of HUVEC cells by ELISA (Figure 5A). Specifically, we focused on HUVECs exposed to CNPI to further understand the molecular mechanism underpinning the angiogenic properties of CNPs. As expected, a significant increase in VEGF levels in culture media in CNPI treated cells was observed with a maximum of VEGF when cells were exposed to a concentration of 1 μM CNPI. Excreted VEGF was less in 2 μM CNP concentration as compared to 1 μM, which indicates 1 μM is an optimum concentration of CNPs required to trigger angiogenesis. Further, intracellular VEGF expression in CNPs treated cells was estimated using western blot as well as RT-PCR technique. VEGF expression was estimated in the whole cell lysate, as a function of time, at an exposure to CNPI at a concentration of 1 μM (Figure 5B). Densitometric analysis of western blot images, normalized to β-actin, showed almost three-fold increase after a 2 h treatment. Similar observations were observed in mRNA expression of VEGF, assayed by quantitative RT-PCR (Figure 5C). From the ELISA, Western blots and RT-PCR data it was clear that exposure of cells to CNPs induces pro-angiogenesis via a VEGF-dependent pathway.

Angiogenesis can be induced either by inducing low levels of intracellular ROS [26] or by controlling the intracellular oxygen concentration to the cells [27]. To identify the pathways by which CNPs induce the angiogenesis, we analyzed intracellular ROS levels using 2′,7′-dichlorodihydrofluorescein diacetate (DCF) (Shown in supplementary document, Figure S3). No increase in ROS generation was observed in CNPI treated cells (green-DCF positive) after 2 h of CNPI treatment. To further confirm we analyzed the mRNA expression of hemeoxygenase-1 (HO-1) and thioredoxin reductase (TrxR1), known to be upregulated during oxidative stress [28, 29]. No increase in HO-1 or TrxR1 expression was observed up

to 4 h after addition of CNPs (Figure S3C). These results indicate that exposure to CNPs does not induce the angiogenesis by triggering higher levels of ROS, unlike Eu(OH)3 nanorods [3, 7] which induces angiogenesis through ROS generation.

On the other hand it is known that angiogenesis can be regulated by tissue local oxygen concentrations. This pathway is indirectly governed by HIF-1α regulation and transcriptional activation of angiogenic factors, which regulates gene expression involved in angiogenesis [11]. Therefore, we estimated the amount of HIF-1α in the cytoplasm and the amount translocated into the nucleus of HUVECs following CNPI treatment. Figure 6A and B present the amount of HIF-1α in cytoplasmic and nuclear fraction in control, CNPI and CoCl$_2$ (Positive control) treated cells [30]. A higher amount of HIF-1α in cytoplasmic fraction was observed in cells treated with CNPI (both 30 min and 2 h treatment) (Figure 6A). **There was a concomitant increase of HIF-1α in the nuclear fraction**. As expected, HIF-1α nuclear translocation was increased in CNPI treated cells (Figure 6B). Figure S4 shows the immunoblotting of nuclear marker histone deacetylase (HDAC-1), which confirmed successful separation of nuclear and cytoplasmic fraction of CNPI treated cells (supplementary document). HIF-1α stabilization and translocation to the nucleus indicates that CNPs induced angiogenesis by regulating HIF-1α.

Immunostaining with pimonidazole was used to determine the intracellular O$_2$ level – an established technique [31]. Immunostaining images representing the intracellular O$_2$ level at different times (30 min, 1 h and 2 h) after CNPI treatment are shown in Figure 6C. Figure 6D shows quantitative immunofluorescence data, which is proportional to the amount of O$_2$. Interestingly, low O$_2$ levels were observed immediately after CNPI treatment up to 1 h, however O$_2$ levels returned to normal after 2 h of CNPI treatment. This supports our hypothesis that CNPs activate HIF-1α by modulation intracellular O$_2$ level.

3.5. Oxygen modulation and surface oxidation state

Our results thus far demonstrated that the Ce^{3+}/Ce^{4+} ratio of the CNP's plays a pivotal role towards angiogenesis. CNPI, with 57 % Ce^{3+} is highly oxygen deficient and therefore we hypothesise that it acts catalytically as an oxygen buffer by providing facile pathways for oxygen modulation. Specifically, CNP's first extract intracellular oxygen and then liberate the oxygen in the catalytic cycle following:

$$CeO_{2-x} + O.5xO_2 \rightleftarrows CeO_2$$
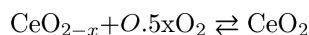
This is supported by our observation of transient hypoxia immediately after CNPI treatment in that the reduced CNP's first deplete oxygen levels. The ease of oxygen extraction from the surface of CNP is central to its catalytic activity and therefore to support our hypothesis we needed to measure the oxygen extraction energy and determine whether the Ce^{3+}/Ce^{4+} ratio influenced this energy. Experimentally this is challenging and therefore we used atomistic computer simulation to calculate the oxygen extraction energy. Migani and co-workers have shown that the oxygen vacancy formation energy is driven by the electrostatics, thus enabling the prediction of the most easily removable oxygen atoms by analyzing the distribution of the electrostatic potential [32].

The atomistic model of a CNP, comprising {100} truncated {111} octahedron (in accord with experiment), is shown in Figure 7(a). Figure 7(b) shows the structure of the nanoparticle with two Ce(IV) atoms, on a {100} surface, reduced to Ce(III). The electrostatic energy maps of the oxygen sublattice for the unreduced and reduced ceria nanoparticles are shown in Figure 7(c&d) using a red-white-blue gradient corresponding to low-high electrostatic energy respectively; regions coloured red are indicative of labile oxygen. Reactivity maps of a model CNP with a high concentration of surface Ce^{3+} species are shown in Figure 7(g, h).

Analysis of the reactivity maps, reveals that oxygen vacancy formation in the vicinity of surface Ce^{3+} is easier, and therefore more reactive towards participating in a catalytic reaction, compared with unreduced areas of the nanoparticle. This finding helps explain why CNP's with a high Ce^{3+}/Ce^{4+} ratio promote angiogenesis and supports our hypothesis that CNPs act catalytically as oxygen buffers by providing facile pathways for intracellular oxygen transport.

CONCLUSION

Summarizing, we have shown that CNPs induce pro-angiogenesis and **this activity** is critically dependent upon the surface valence states. In particular, reduced CNPs induced endothelial cell proliferation, and tube formation in *in vitro* **cell culture** and vascular sprouting *in vivo.* Moreover, CNPs stabilized HIF-1α in endothelial cells and altered gene regulation, which induced pro-angiogenesis. The Ce^{3+}/Ce^{4+} ratio and particle size was key to pro-angiogenesis enabling the CNPs to act catalytically as oxygen modulators by providing facile pathways for the liberation and replenishment of intracellular oxygen.

Supplementary Material

Refer to Web version on PubMed Central for supplementary material.

Acknowledgments

References

1. Baker M, Robinson SD, Lechertier T, Barber PR, Tavora B, D'Amico G, et al. Use of the mouse aortic ring assay to study angiogenesis. Nat Protocols. 2011; 7:89–104. [PubMed: 22193302]

2. Chung AS, Lee J, Ferrara N. Targeting the tumour vasculature: insights from physiological angiogenesis. Nat Rev Cancer. 2010; 10:505–514. [PubMed: 20574450]

3. Patra CR, Kim J-H, Pramanik K, d'Uscio LV, Patra S, Pal K, et al. Reactive Oxygen Species Driven Angiogenesis by Inorganic Nanorods. Nano Lett. 2011; 11:4932–4938. [PubMed: 21967244]

4. Leung K-W, Ng H-M, Tang M, Wong C, Wong R, Wong A. Ginsenoside-Rg1 mediates a hypoxia-independent upregulation of hypoxia-inducible factor-1α to promote angiogenesis. Angiogenesis. 2011; 14:515–522. [PubMed: 21964931]

5. Yoshida S, Ono M, Shono T, Izumi H, Ishibashi T, Suzuki H, et al. Involvement of interleukin-8, vascular endothelial growth factor, and basic fibroblast growth factor in tumor necrosis factor alpha-dependent angiogenesis. Mol Cell Biol. 1997; 17:4015–4023. [PubMed: 9199336]

6. Claffey KP, Brown LF, del Aguila LF, Tognazzi K, Yeo K-T, Manseau EJ, et al. Expression of Vascular Permeability Factor/Vascular Endothelial Growth Factor by Melanoma Cells Increases Tumor Growth, Angiogenesis, and Experimental Metastasis. Cancer Res. 1996; 56:172–181. [PubMed: 8548760]

7. Patra CR, Bhattacharya R, Patra S, Vlahakis NE, Gabashvili A, Koltypin Y, et al. Pro-angiogenic Properties of Europium(III) Hydroxide Nanorods. Adv Mater. 2008; 20:753–756.

8. Celardo I, Pedersen JZ, Traversa E, Ghibelli L. Pharmacological potential of cerium oxide nanoparticles. Nanoscale. 2011; 3:1411–1420. [PubMed: 21369578]

9. Jia C-J, Schuth F. Colloidal metal nanoparticles as a component of designed catalyst. Phys Chem Chem Phys. 2011:13.

10. Campbell CT, Peden CHF. Oxygen Vacancies and Catalysis on Ceria Surfaces. Science. 2005; 309:713–714. [PubMed: 16051777]

11. Han J-Y, Oh SH, Morgillo F, Myers JN, Kim E, Hong WK, et al. Hypoxia-inducible Factor 1alpha and Antiangiogenic Activity of Farnesyltransferase Inhibitor SCH66336 in Human Aerodigestive Tract Cancer. J Natl Cancer Inst. 2005; 97:1272–1286. [PubMed: 16145048]

12. Hirst SM, Karakoti AS, Tyler RD, Sriranganathan N, Seal S, Reilly CM. Anti-inflammatory Properties of Cerium Oxide Nanoparticles. Small. 2009; 5:2848–2856. [PubMed: 19802857]

13. Vlahakis NE, Young BA, Atakilit A, Hawkridge AE, Issaka RB, Boudreau N, et al. Integrin alpha9beta1 Directly Binds to Vascular Endothelial Growth Factor (VEGF)-A and Contributes to VEGF-A-induced Angiogenesis. J Biol Chem. 2007; 282:15187–1596. [PubMed: 17363377]

14. Fang J, Shing Y, Wiederschain D, Yan L, Butterfield C, Jackson G, et al. Matrix metalloproteinase-2 is required for the switch to the angiogenic phenotype in a tumor model. Proc Natl Acad Sci U S A. 2000; 97:3884–3889. [PubMed: 10760260]

15. Varia MA, Calkins-Adams DP, Rinker LH, Kennedy AS, Novotny DB, Fowler WC Jr, et al. Pimonidazole: A Novel Hypoxia Marker for Complementary Study of Tumor Hypoxia and Cell Proliferation in Cervical Carcinoma. Gynecol Oncol. 1998; 71:270–277. [PubMed: 9826471]

16. Smith, W.; Forester, TR. DL_POLY: copyright by the council for the Central Laboratory of the Research Councils. Daresbury Laboratory; Daresbury, Warrington, UK: 1996.

17. Sayle TXT, Parker SC, Catlow CRA. The role of oxygen vacancies on ceria surfaces in the oxidation of carbon monoxide. Surf Sci. 1994; 316:329–336.

18. Feng X, Sayle DC, Wang ZL, Paras MS, Santora B, Sutorik AC, et al. Converting Ceria Polyhedral Nanoparticles into Single-Crystal Nanospheres. Science. 2006; 312:1504–1508. [PubMed: 16763144]

19. Zhang J, Kumagai H, Yamamura K, Ohara S, Takami S, Morikawa A, et al. Extra-Low-Temperature Oxygen Storage Capacity of CeO2 Nanocrystals with Cubic Facets. Nano Lett. 2011; 11:361–364. [PubMed: 21204550]

20. Deshpande S, Patil S, Kuchibhatla SV, Seal S. Size dependency variation in lattice parameter and valency states in nanocrystalline cerium oxide. Appl Phys Lett. 2005; 87:133113.

21. Kuchibhatla SVNT, Karakoti AS, Sayle DC, Heinrich H, Seal S. Symmetry-Driven Spontaneous Self-Assembly of Nanoscale Ceria Building Blocks to Fractal Superoctahedra. Cryst Growth Des. 2009; 9:1614–1620.

22. Recillas S, Colón J, Casals E, González E, Puntes V, Sánchez A, et al. Chromium VI adsorption on cerium oxide nanoparticles and morphology changes during the process. J Hazard Mater. 2010; 184:425–431. [PubMed: 20832170]

23. Karakoti AS, Kuchibhatla SVNT, Baer DR, Thevuthasan S, Sayle DC, Seal S. Self-Assembly of Cerium Oxide Nanostructures in Ice Molds. Small. 2008; 4:1210–1216. [PubMed: 18654994]

24. Fosbrink M, Niculescu F, Rus V, Shin ML, Rus H. C5b-9-induced Endothelial Cell Proliferation and Migration Are Dependent on Akt Inactivation of Forkhead Transcription Factor FOXO1. J Biol Chem. 2006; 281:19009–190018. [PubMed: 16670089]

25. McGonigle, S.; Shifrin, V. Current Protocols in Pharmacology. John Wiley & Sons, Inc; 2001. In Vitro Assay of Angiogenesis: Inhibition of Capillary Tube Formation.

26. Ushio-Fukai M. Redox signaling in angiogenesis: Role of NADPH oxidase. Cardiovasc Res. 2006; 71:226–235. [PubMed: 16781692]

27. Facciabene A, Peng X, Hagemann IS, Balint K, Barchetti A, Wang L-P, et al. Tumour hypoxia promotes tolerance and angiogenesis via CCL28 and Treg cells. Nature. 475:226–230. [PubMed: 21753853]

28. Ferguson HE, Thatcher TH, Olsen KC, Garcia-Bates TM, Baglole CJ, Kottmann RM, et al. Peroxisome proliferator-activated receptor-γ ligands induce heme oxygenase-1 in lung fibroblasts by a PPARγ-independent, glutathione-dependent mechanism. American Journal of Physiology - Lung Cellular and Molecular Physiology. 2009; 297:L912–L9. [PubMed: 19734319]

29. Park YS, Taniguchi N. Acrolein Induces Inflammatory Response Underlying Endothelial Dysfunction. Annals of the New York Academy of Sciences. 2008; 1126:185–189. [PubMed: 18448814]

30. Garedew A, Moncada S. Mitochondrial dysfunction and HIF1α stabilization in inflammation. Journal of Cell Science. 2008; 121:3468–3475. [PubMed: 18827009]

31. Doege K, Heine S, Jensen I, Jelkmann W, Metzen E. Inhibition of mitochondrial respiration elevates oxygen concentration but leaves regulation of hypoxia-inducible factor (HIF) intact. Blood. 2005; 106:2311–2317. [PubMed: 15947089]

32. Migani A, Vayssilov GN, Bromley ST, Illas F, Neyman KM. Dramatic reduction of the oxygen vacancy formation energy in ceria particles: A possible key to their remarkable reactivity at the nanoscale. J Mater Chem. 2010; 20:10535–10546.
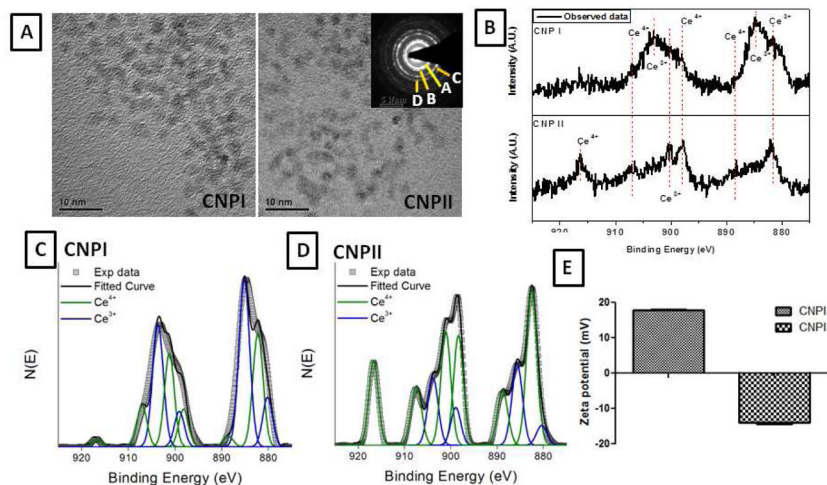
Figure 1.
Characterization of synthesized CNPs. Figure 1A shows HRTEM image of differently engineered cerium oxide nanoparticles (CNP I & II), having similar shape and size (3–5nm). In the inset selected area electron diffraction (SAED) pattern confirms the fluorite structure and A (100), B (200), C (220), D (311) are the crystal plane of the lattice. XPS spectrum of CNPI & II is shown in Figure 1B. Figure 1C & D shows deconvoluted XPS spectra of CNPI and CNPII. Zeta potential of both the CNPs is shown in figure 1E.
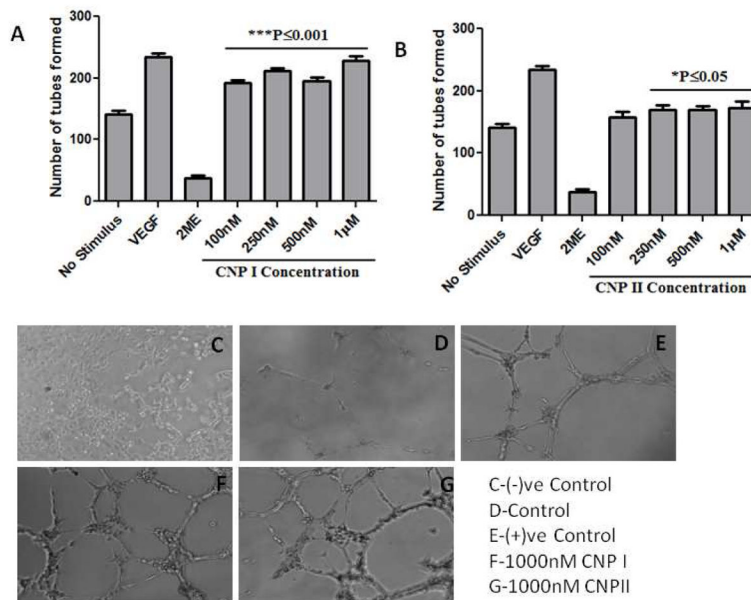
Figure 2.
CNPs induce angiogenesis in HUVEC cell culture model. HUVEC cells were cultured with vehicle (control), 10μM β-estradiol (negative control), 30ng rVEGF (positive control) and varying concentrations of cerium oxide nanoparticles (100nM to 1μM CNPI or CNPII) and tube formation counted as the number of branches at 10X magnification after 8hr of treatment. Data represents the mean of at least six different experiments and the plotted error represents the standard deviation. Number of tubes formed when cells were exposed to different concentrations of CNPI and CNPII is shown in panels A and B respectively. Images of tubes formed in beta-estradiol (C), control (D), VEGF treated (E), 1μM CNPI treated (F) and 1000 nM CNPII treated (G) after 8 hr of incubation are shown.
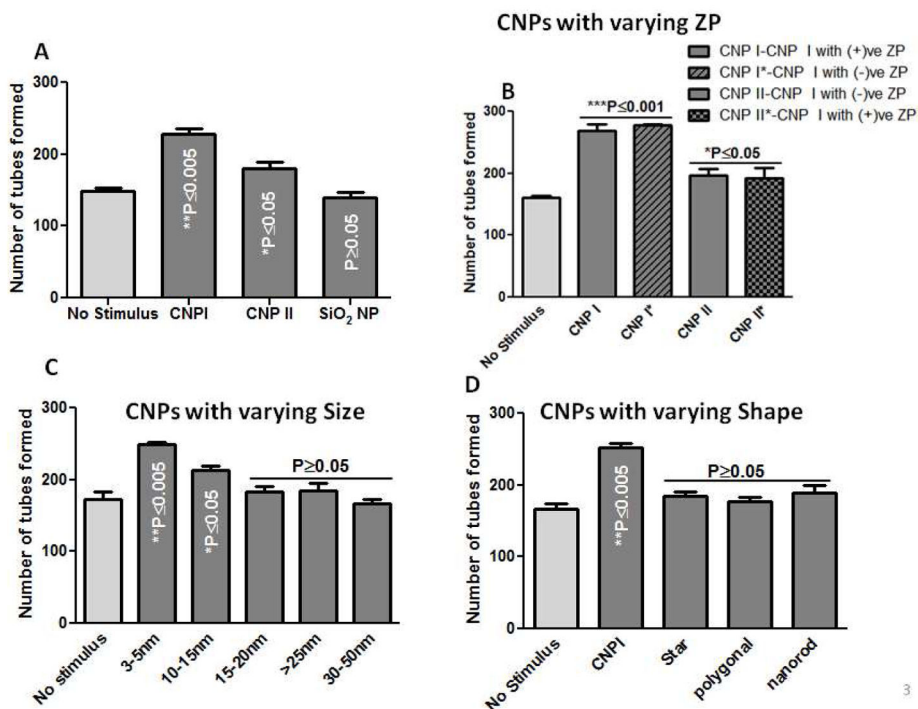
Figure 3.
Effect of different Ce^{3+}/Ce^{4+} ratio, zeta potential, size and shape of CNPs on tube formation. Tube formation in (A) CNP I ($Ce^{3+}/Ce^{4+} \rightarrow 1.33$), CNP II ($Ce^{3+}/Ce^{4+} \rightarrow 0.37$) and SiO_2; (B) CNP with different zeta potentials: CNPI ($+17.78\pm0.5$mV), CNP I′ (-20 ± 1.4mV), CBP II (-14.05 ± 0.83mV) and CNP II′ ($+34.05\pm0.52$mV); (C) CNPs with varying size; (D) CNPs with varying shape. All the experiments were carried out with cells exposed to nanoparticles at a concentration of 1μM. Data represents a mean of at least six experiments and the error plotted represents the standard deviation.
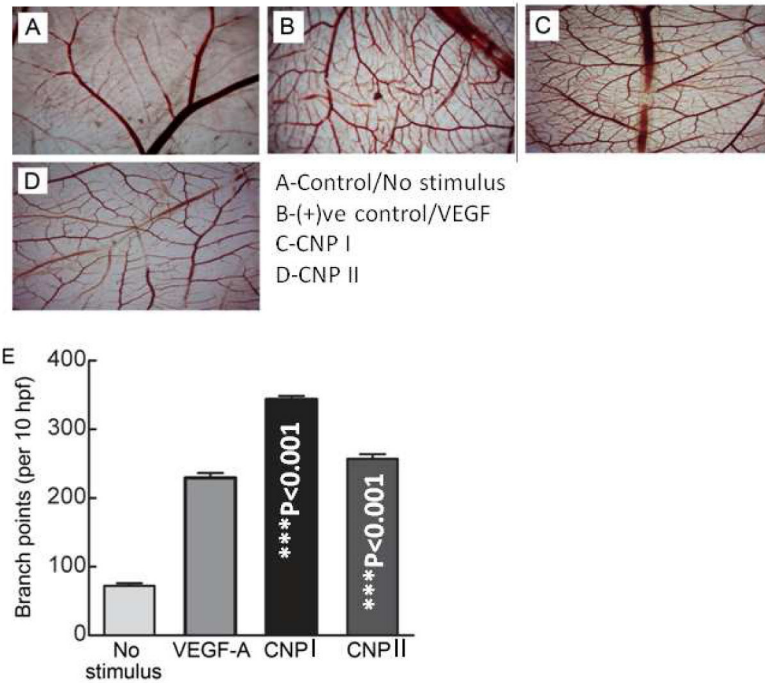
Figure 4.
CNPs induce vascular sprouting in CAM assay. Nanoparticle-induced angiogenesis measured by Chick CAM assay (A–D). The extent of angiogenesis on CAM's treated with either (A) methylcellulose, (B) 50 ng of VEGF-A, (C) 1μg of CNP1 or (D) 1μg of CNP2. (E) The extent of CAM angiogenesis measured by counting the number of vascular sprouts from tertiary vessels in a minimum of 8 separate experiments. Hpf: high power field.
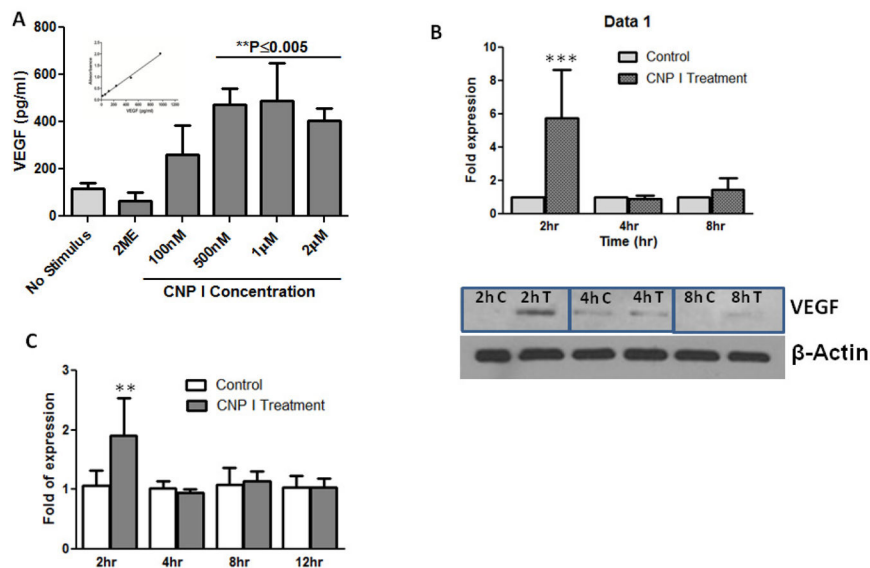
Figure 5.
CNPs mediated induction of VEGF expression. (A) Amount of VEGF released from HUVEC cells to culture supernatant (exposed to varying concentrations of CNPI) were measured by using ELISA; (B) Intracellular VEGF levels from HUVEC cells after CNPI treatment (for different time points) was analyzed using western blot. Semi-quantitative data obtained by densitometric analysis of western blot images are presented as mean ± standard deviation from multiple experiments; (C) Changes in HUVEC cell m-RNA level after CNPI treatment were determined by RT-PCR as described in methods.
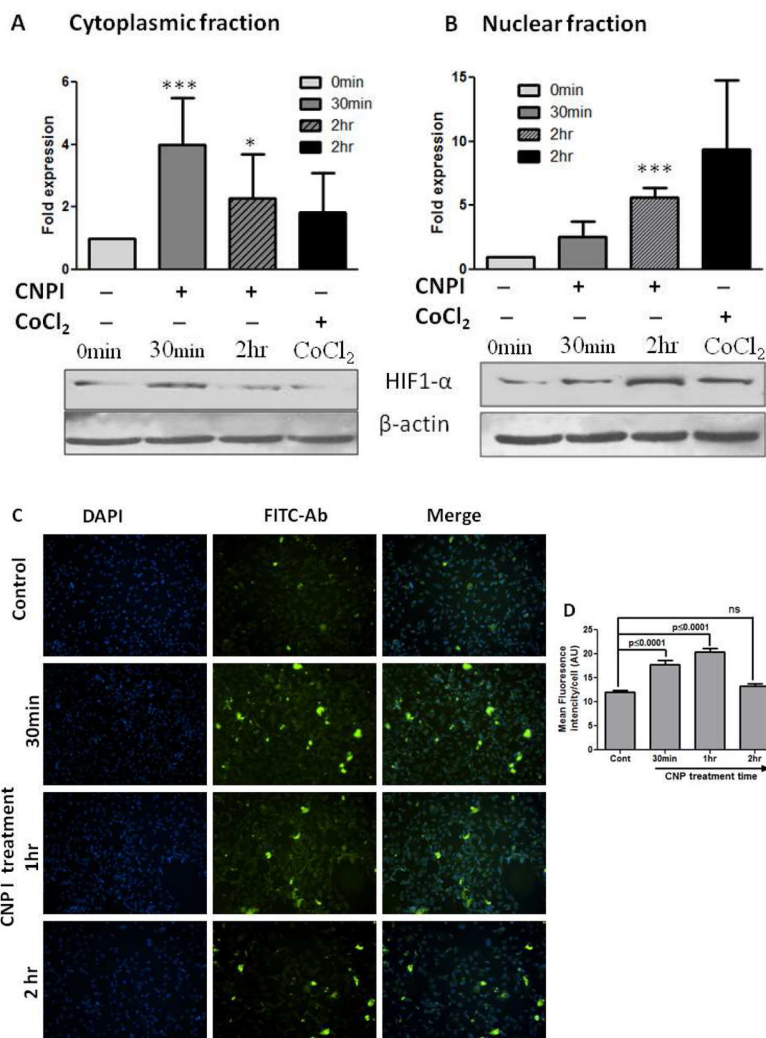
Figure 6.
CNPs mediated regulation of HIF1 α by altering the intracellular oxygen concentration. Analysis of HIF1α in cytoplasmic (A) and nuclear (B) fractions at different time points (0min, 30min and 2hr) in cells treated with 1μM CNPI or $CoCl_2$ used as a positive control (2hr). Semi-quantitative data obtained by densitometric analysis are presented as mean ± standard deviations from two independent experiments. The bar diagram is the fold of HIF1α amount as normalized to the β-actin expression. Panel C shows the immunofluorescence image (left to right: Blue- DCF, Green-pimonidazole staining and merge image) of control and CNP treated HUVEC cells for different time durations (0min, 30min, 2hr). The semi-quantitative data (D) calculated by measuring the fluorescence intensity of cells and presented as mean ± standard deviations.
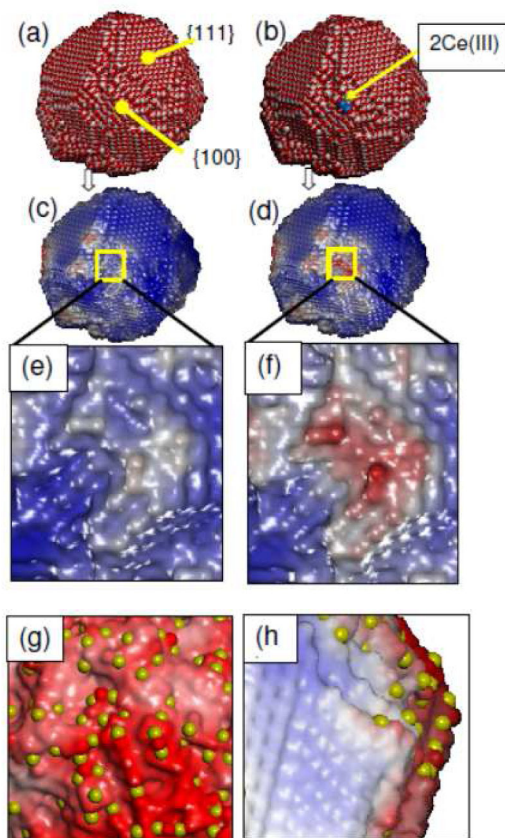
Figure 7.
Atomistic models and (oxygen) electrostatic energy surfaces for CeO2 nanoparticles (CNP). Sphere model representation of the atom positions comprising (a) the unreduced ceria NP and (b) reduced ceria NP. Oxygen is coloured red, Ce4+ is white and Ce3+, blue. (c) and (d) show the electrostatic energy surface map of the unreduced and reduced ceria NP's respectively and enlarged in (e) and (f). (g) and (h) show an area of a CNP with a high concentration of Ce3+ ions (yellow spheres) on the surface. Domains in the vicinity of Ce3+ are red indicating labile oxygen, conversely domains relatively devoid of surface Ce3+ are blue indicating a reduced reactivity towards oxygen extraction. Red-white-blue gradient scale indicates low to high electrostatic energy respectively; low electrostatic energy (coloured red) is indicative of labile oxygen.

Table 1

Real-Time PCR Primers, listed 5′ to 3′

Genes	Primer Sequence
HO-1 forward	5′-CTGAGTTCATGAGGAACTTTCAGAAG-3′
HO-1 reverse	5′-TGGTACAGGGAGGCCATCAC-3′
Trx forward	5′-GCAGATCGAGAGCAAGACTG-3′
Trx reverse	5′-CTCCAGAAAATTCACCCACC-3′
VEGF forward	5′-ACACATTGTTGGAAGAAGCAGCCC-3′
VEGF reverse	5′-AGGAAGGTCAACCACTCACACACA-3′
GAPGH forward	5′-AGTAGAGGCAGGGATGATGTT-3′
GAPDH reverse	5′-CTTTGGTATCGTGGAAGGACTC-3′

Table 2

Model parameters used to describe CeO_2

Atom i	Atom j	A (eV)	ρ(Å)	C (eV.Å⁶)	Cut-off (Å)
O	O	22764.30	0.149	27.89	10.0
O	Ce(IV)	1986.83	0.351	20.40	10.0
O	Ce(III)	1731.62	0.364	14.43	10.0

Atom	Mass (amu)	Charge (e)
O	16.00	−2.0
Ce(IV)	140.12	+4.0
Ce(III)	140.12	+3.0

All other interactions set to zero